Grain Boundary Structure-Property Model Inference Using Polycrystals: The Overdetermined Case

Christian Kurniawan[a,b], Sterling Baird[a], David T. Fullwood[a], Eric R. Homer[a], Oliver K. Johnson[a,*]

[a]*Department of Mechanical Engineering, Brigham Young University, Provo, UT 84602, USA*
[b]*Department of Materials Science and Engineering, Carnegie Mellon University, Pittsburgh, PA 15213, USA*

Abstract

Efforts to construct predictive grain boundary (GB) structure-property models have historically relied on property measurements or calculations made on *bicrystals*. Experimental bicrystals can be difficult or expensive to fabricate, and computational constraints limit atomistic bicrystal simulations to high symmetry GBs (i.e. those with small enough GB periodicity). Although the use of bicrystal property data to construct GB structure-property models is more direct, in many experimental situations the only type of data available may be measurements of the effective properties of polycrystals. In this work, we investigate the possibility of inferring GB structure-property models from measurements of the homogenized effective properties of polycrystals *when the form of the structure-property model is unknown*. We present an idealized case study in which GB structure-property models for diffusivity are inferred from noisy simulation results of two-dimensional microstructures, under the assumption that the number of polycrystal measurements available is larger than the number of parameters in the inferred model. We also demonstrate how uncertainty quantification for the inferred structure-property models is easily performed within this framework.

Keywords: Grain Boundary, Structure-Property Model, Inference, Uncertainty Quantification, Inverse Problem

1. Introduction

Efforts to develop grain boundary (GB) structure-property models have historically relied on experiments or atomistic calculations performed on bicrystals [1–4]. However, due to the high dimensionality of the GB configuration space, measuring and/or calculating GB properties one-by-one has limited the scope of investigations primarily to a relatively small set of highly symmetric GB types [5]. This has greatly hampered the development of GB structure-property models and, at present, prediction of GB properties as a function of their crystallography is only possible for a small number of properties [6, 7].

While the use of bicrystal data to construct GB structure-property models is the most direct route, bicrystals are not always available; rather, the most ubiquitous microstructures are polycrystalline and data for the effective (homogenized) properties of polycrystals may be the only data available in many situations. Thus, we ask the question, "If I only have access to polycrystals, would it be possible to use them to infer GB structure-property models?" While one might intuitively anticipate an affirmative answer to this question, the challenge for such an approach lies in the deconvolution of the respective contributions of each GB to the measured effective property of the polycrystal (which is the observed data that is available).

*Corresponding author.
Email address: ojohnson@byu.edu (Oliver K. Johnson)

Because it is the inverse of the problem of *homogenization*, we refer to this problem of inferring constituent properties from the effective properties of a material as *property localization*[1]. Previous examples of localization problems in the literature have focused on obtaining single crystal elastic constants from measurements of the elastic response of polycrystals [15–25].

We have recently applied the property localization concept to GBs to infer the parameters of a structure-property model for GB diffusivity from synthetic idealized two-dimensional polycrystals with honeycomb geometry [26]. In that prior work, the inverse problem of GB property localization was solved by regression with an analytical *ansatz* (i.e. the form of the structure-property model was known *a priori*). Although successful, the requirement of an explicit analytical *ansatz* is a significant limitation because for many GB properties, including diffusivity, the functional form of the structure-property model is unknown; in fact, the model form is precisely the information one hopes to learn by the inference effort.

In this work, we develop a new approach for GB property localization based on Bayesian strategies employed in geostatistics. In addition to eliminating the requirement for an analytical *ansatz*, our new method naturally facilitates uncertainty quantification for the inferred structure-property model. In short, our method allows one to characterize polycrystalline samples, measure their effective (macroscopic) properties, and from this information determine the properties of the constituent GBs without any *a priori* knowledge about the form of the underlying structure-property model and with rigorously quantified uncertainty. We will focus here on the overdetermined case: when the number of available polycrystal measurements is larger than the number of values/parameters to be inferred. This is likely to be the case when the GB property depends, at least approximately, on only one or a small subset of the crystallographic GB parameters (e.g. the disorientation angle, or the GB plane). In a sequel to this paper we address the underdetermined case, the solution of which is an extension of the mathematical tools developed here. To validate our new approach, we infer structure-property models for GB diffusivity from calculations of the effective diffusivity of realistic two-dimensional polycrystals, without the need for *a priori* information about the form of the constitutive models. By enabling the use of simple to manufacture, and abundantly available polycrystals (instead of reliance on bicrystals), we anticipate that this new strategy will assist in the problem of inferring structure-property models for GBs.

2. Methods

The goal of this study is to develop a new GB property localization method to infer structure-property models for GB diffusivity from the effective diffusivity of polycrystals. In the present work, we describe the relevant theory and demonstrate its application for an idealized model system, in an effort to validate the approach. The paper is organized as follows: Section 2.1 describes the synthetic microstructures used in this work; Section 2.2 outlines how the effective grain boundary network diffusivity is calculated; Sections 2.3 and 2.4 describe the theory of property localization, including corresponding uncertainty quantification; and in Section 3 we present and discuss our results.

2.1. Microstructures

We generated 2D polycrystalline microstructures using the method of Johnson, et al. [27]. Each microstructure is the result of an isotropic grain growth simulation performed using a front-tracking

[1] We use the term "property localization" to distinguish this problem from the more frequently studied problem of inferring the local state (e.g. the local stress tensor) from the macroscopic state (e.g. the effective stress tensor) of a polycrystal [8–14], which we refer to as "state localization".

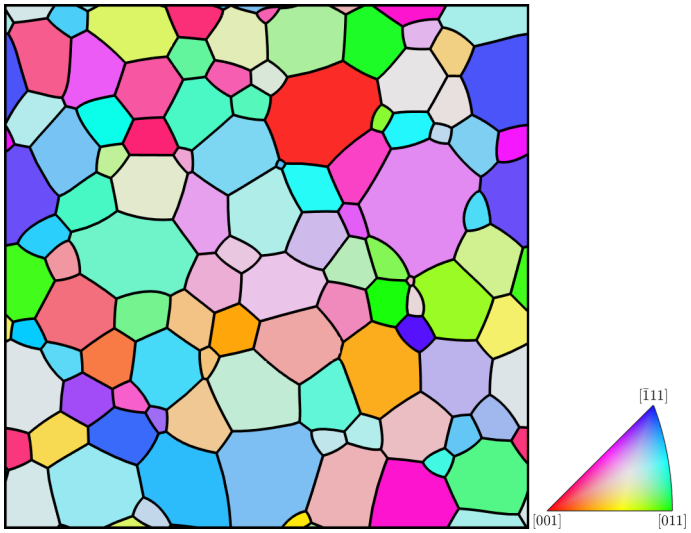

Figure 1: Example of a two-dimensional polycrystal template used in this study. Colors indicate crystallographic orientation, as shown in the accompanying inverse pole figure (IPF) color legend.

algorithm [28] (code written by Jeremy Mason[2]). Each simulation was initialized with a Voronoi microstructure constructed from randomly generated uniformly distributed seeds and resulting in 1000 cells (*i.e.* grain precursors). We allowed the microstructure to evolve under mean curvature flow until about 100 grains remained. We then assigned grain orientations according to the simulated annealing procedure described in [27] which ensures that the generated polycrystals span the space of possible triple-junction fractions[3] in order to encourage diversity of the grain boundary network (GBN) structure in the resulting pool of microstructures. An example microstructure generated by this procedure is shown in Fig. 1. A pool of 1771 polycrystals was generated spanning the space of triple-junction fractions, from which representatives were selected uniformly at random during the inference process.

2.2. Homogenization

For each microstructure, the effective diffusivity of the GBN is calculated via (see Appendix A)

$$\bar{D}^{\text{pred}}(\mathscr{D}, M) = -\frac{L}{A}\mathcal{L}_b^{\intercal}\widehat{\mathcal{L}}^{-1}e_b \tag{1}$$

where $\bar{D}^{\text{pred}}$ is the effective diffusivity; M abstractly represents the relevant microstructural information (*i.e.* the character and arrangement of the GBs in the present application); $\mathscr{D}$ is a function that abstractly represents the GB diffusivity structure-property model; L and A are the length and cross-sectional area of the polycrystal, respectively; $\mathcal{L}_b$ is the b-th column of the diffusivity-weighted GBN Laplacian matrix ($\mathcal{L}$), which encodes the topology of the GBN and the diffusivity of each GB [27]; e_b is a vector whose b-th element is 1, all others being 0; and $\widehat{\mathcal{L}}$ is a modified version of $\mathcal{L}$, in which the a-th and b-th rows are replaced by $e_a^{\intercal}$ and $e_b^{\intercal}$, respectively, and where a and b are the indices of the diffusivity source and sink nodes respectively (the left and right sides, respectively, of the microstructures in our study).

[2]The code implements the method established by [28], and is available at `http://mason.mse.ucdavis.edu/wp-content/uploads/2018/01/FTGG2_v1_0.zip`.

[3]Triple junction fractions, J_0, J_1, J_2, and J_3, represent the population of GB triple junctions coordinated by $0, 1, 2$, or 3 "special" GBs, respectively. Further discussion about triple junction fractions can be found in [29–34].

For our synthetic microstructures, Eq. 1 is exact. However, in practical applications, one would employ digital representations of microstructures acquired from, *e.g.*, electron backscatter diffraction (EBSD) measurements, and property measurement techniques with finite resolution. To simulate uncertainties that would arise from measurement uncertainty, we add Gaussian noise such that the observed effective diffusivity ($\bar{D}^{\text{obs}}$) is given by:

$$\bar{D}^{\text{obs}} = \bar{D}^{\text{pred}} + \epsilon \tag{2}$$

where $\epsilon \sim N\left[0, \left(1\% \left(\bar{D}^{\text{pred}}\right)\right)^2\right]$. The uncertainty in microstructure characterization via EBSD is negligible [35–39] compared to the uncertainty in typical measurements of diffusivity. Consequently, we do not add any noise to M, but treat it exactly.

With both $\bar{D}^{\text{obs}}$ and M being measured, the unknown in Eq. 1 is the structure-property model, $\mathscr{D}$, which we seek to infer using the tools of Bayesian inverse problem theory. For the purposes of validation, we assign GB diffusivities using a hypothetical constitutive model. Because no general structure-property models for GB diffusivity currently exist[4], we employ the function developed by Bulatov, Reed, and Kumar to describe GB energy [7], but we map it to the range of realistic values of GB diffusivity as described later; we will refer to this as the BRK model. With GB diffusivities assigned, we then calculate the effective diffusivity using the procedure already described, including the introduction of noise. During the inference process, we ignore any knowledge of the assigned constitutive model and consider only M and $\bar{D}^{\text{obs}}$ as the input variables. Validation of the inference method then consists of comparing the actual constitutive model with the inference result.

2.3. GB Property Localization

In this section, we describe how GB property localization is performed in general, and then how a Bayesian approach to inverse problem theory may be applied in this context. GB property localization [26] consists of first characterizing the microstructures of a set of polycrystals (*e.g.* via EBSD). The resulting microstructural information is denoted $\mathbf{M} = \{M_1, M_2, ..., M_N\}$, where M_i describes the i-th microstructure. Measurements are then performed to determine the relevant effective property of each polycrystal. In the present case we are interested in the effective diffusivity, $\bar{\mathbf{D}}^{\text{obs}} = \{\bar{D}_1^{\text{obs}}, \bar{D}_2^{\text{obs}}, ..., \bar{D}_N^{\text{obs}}\}$. The relevant homogenization relation, Eq. 1, is then inverted to determine the unknown structure-property model, $\mathscr{D}$.

Here, we propose the use of a Bayesian framework to perform the homogenization inversion step to solve for the unknown structure-property model. The formalism developed by Tarantola, Valette, and Mosegaard [42–44] allows us to describe our "state of information" (what we know) about $\mathscr{D}$ after making our measurements of $\mathbf{M}$ and $\bar{\mathbf{D}}^{\text{obs}}$ using the following probability density function, or PDF (see Appendix B for a complete derivation):

$$\sigma(\mathscr{D}, \mathbf{M}) \propto \rho_{\{\mathscr{D},\mathbf{M}\}}\left(\mathscr{D}, \mathbf{M}\right) \rho_{\bar{\mathbf{D}}^{\text{obs}}}\left(\bar{\mathbf{D}}^{\text{pred}}(\mathscr{D}, \mathbf{M})\right) \tag{3}$$

Here, $\sigma(\mathscr{D}, \mathbf{M})$ is the *a posteriori* joint probability density of $\mathscr{D}$ and $\mathbf{M}$; $\rho_{\{\mathscr{D},\mathbf{M}\}}\left(\mathscr{D}, \mathbf{M}\right)$ is the *a priori* state of information about $\mathscr{D}$ and $\mathbf{M}$; and $\rho_{\bar{\mathbf{D}}^{\text{obs}}}\left(\bar{\mathbf{D}}^{\text{pred}}(\mathscr{D}, \mathbf{M})\right)$ is a likelihood function which quantifies how well the model explains the data. With $\mathbf{M}$ and $\bar{\mathbf{D}}^{\text{obs}}$ obtained via measurement, we infer the unknown structure-property model for GB diffusivity ($\mathscr{D}$) by determining, among all possible models, the one that maximizes $\sigma(\mathscr{D}, \mathbf{M})$. We wish to do this without an *ansatz* for the model form, so that both

[4] In the absence of a measured structure-property model, computational studies have typically employed a discrete binary model with low- and high-angle GBs possessing different constant values of properties [26, 40], though there are some studies that have employed continuous functions (see [41] for an example).

the form and any model parameters are dictated by the observed data. As will be described below, we accomplish this by first discretizing the domain of $\mathscr{D}$, then describing the *a priori* state of information by appropriate PDFs, and finally, solving an optimization problem with Eq. 3 as the objective function to infer the value of the diffusivity structure-property model at specific points over the domain, thus obtaining a piece-wise linear approximation to $\mathscr{D}$.

Because we wish to infer the structure-property model without *a priori* knowledge of its form, we discretize the GB character space so that $\mathscr{D}$ will be approximated as a piece-wise linear function with unknown parameters $\mathbf{D} = \{D_1, D_2, ..., D_J\}$, where the D_j are the diffusivities at locations across the domain that will be specific to the particular discretiztaion employed. The only *a priori* information about the model parameters that we consider is that the diffusivity is everywhere non-negative (*i.e.* we assume that no spinodal-type phase transformation is occurring). This prior knowledge can be expressed probabilistically by setting the probability density to zero for any model containing any elements of $\mathbf{D}$ that are negative:

$$\rho_{\mathscr{D}}(\mathbf{D}) = \begin{cases} 1, & D_j \geq 0, \forall\ j \in [1, J] \\ 0, & \text{otherwise} \end{cases} \tag{4}$$

Because we are using simulated polycrystals, our *a priori* knowledge of each microstructure is exact. Technically this implies a generalized Dirac delta function, $\delta(\mathbf{M}', \mathbf{M})$, for the *a priori* state of information about $\mathbf{M}$; however, because the zero value of such a function would be reserved for conditions that, by definition, can never be satisfied, it is sufficient to define $\rho_{\mathbf{M}}(\mathbf{M}) = 1$. If experimental samples were considered, this assumption would also be a reasonable approximation if the measurement uncertainty for the microstructure characterization was small compared to other sources of uncertainty—which is often the case—otherwise, their $\rho_{\mathbf{M}}(\mathbf{M})$ would need to be represented by a distribution whose dispersion encoded the uncertainty resulting from the characterization procedure. We have hitherto referred abstractly to $\mathbf{M}$ as containing some information about the state of the microstructure. This is because for property localization in general, different properties of interest may depend on the character/state of different microstructural features (e.g. composition, phase fractions, phase morphology, crystallographic texture). The details about what information is contained in $\mathbf{M}$ and how it is represented are therefore problem specific, but the methods presented here are quite general. For the present problem, $\mathbf{M}$ contains the character and arrangement of the GBs in the microstructure, explicitly given by the GBN Laplacian, $\mathcal{L}$, described in Section 2.2.

The independence of $\mathbf{D}$ and $\mathbf{M}$ implies that their joint distribution is given by:

$$\rho_{\{\mathscr{D},\mathbf{M}\}}(\mathbf{D}, \mathbf{M}) = \rho_{\mathscr{D}}(\mathbf{D})\rho_{\mathbf{M}}(\mathbf{M}) \tag{5}$$

Finally, for each polycrystal, we represent the likelihood function by a Gaussian-like PDF:

$$\rho_{\bar{\mathbf{D}}^{\text{obs}}}\left(\bar{D}^{\text{pred}}(\mathbf{D}, M_i)\right) \propto \exp\left(-\frac{\left(\bar{D}_i^{\text{obs}} - \bar{D}^{\text{pred}}(\mathbf{D}, M_i)\right)^2}{2s_i^2}\right) \tag{6}$$

where, s_i characterizes the measurement uncertainty of $\bar{D}_i^{\text{obs}}$, which, in the present case, is equal to the standard deviation of the noise we introduced (*i.e.* $s_i = 1\%\bar{D}^{\text{pred}}(\mathscr{D}, M_i)$). Because we assume that we only know $\bar{\mathbf{D}}^{\text{obs}}$ (not $\bar{\mathbf{D}}^{\text{pred}}$), we estimate the value of s_i as $s_i \approx 1\%\left(\bar{D}_i^{\text{obs}}\right)$. Considering all of the microstructures together we have, again because of independence, the joint distribution

$$\rho_{\bar{\mathbf{D}}^{\text{obs}}}\left(\bar{\mathbf{D}}^{\text{pred}}(\mathbf{D}, \mathbf{M})\right) \propto \exp\left(-\sum_{i=1}^{N}\frac{\left(\bar{D}_i^{\text{obs}} - \bar{D}^{\text{pred}}(\mathbf{D}, M_i)\right)^2}{2s_i^2}\right) \tag{7}$$

This implies that when a model ($\mathbf{D}$) is considered that minimizes the difference between $\bar{\mathbf{D}}^{\text{obs}}$ and $\bar{\mathbf{D}}^{\text{pred}}(\mathbf{D}, \mathbf{M})$, the likelihood will be maximized and such a model would best explain the observed data.

Substituting Eqs. 5 and 7 into Eq. 3, with $\mathbf{D}$ representing the discrete approximation to $\mathscr{D}$, we obtain the *a posteriori* state of information for the independent parameters:

$$\sigma\left(\mathbf{D}, \mathbf{M}\right) \propto \begin{cases} \exp\left(-\sum_{i=1}^{N} \frac{\left(\bar{D}_i^{\text{obs}} - \bar{D}^{\text{pred}}(\mathbf{D}, M_i)\right)^2}{2s_i^2} \right), & \mathbf{D} \geq 0 \\ 0, & \text{otherwise} \end{cases} \tag{8}$$

With an expression for the *a posteriori* state of information in hand we are now in a position to perform the inversion of the homogenization equation to infer the approximation of $\mathscr{D}$. This is accomplished by maximizing $\sigma\left(\mathbf{D}, \mathbf{M}\right)$, with the D_j as the design variables:

$$\mathbf{D} = \arg\max_{\mathbf{D}} \sigma\left(\mathbf{D}, \mathbf{M}\right) \tag{9}$$

Because the form of Eq. 8 is a multivariate Gaussian, the maximum coincides with the center of the distribution, whose location occurs at [44]:

$$\mathbf{D} = \left(\mathbf{G}^{\intercal}\mathbf{C}^{-\mathbf{1}}_{\bar{\mathbf{D}}^{\text{obs}}}\mathbf{G}\right)^{-\mathbf{1}} \left(\mathbf{G}^{\intercal}\mathbf{C}^{-\mathbf{1}}_{\bar{\mathbf{D}}^{\text{obs}}}\bar{\mathbf{D}}^{\text{obs}}\right) \tag{10}$$

where $C^{ij}_{\bar{\mathbf{D}}^{\text{obs}}} = s_i\delta_{ij}$ is the covariance matrix of the observed effective diffusivities, and

$$G_{ij} = \left.\frac{\partial \bar{D}^{\text{pred}}(\mathbf{D}, M_i)}{\partial D_j}\right|_{\mathbf{D}} \tag{11}$$

is the matrix of partial functional (Fréchet) derivatives. Note that because Eq. 11 is evaluated at the point $\mathbf{D}$ in the model space, this implies that Eq. 10 is an implicit equation. To solve this equation we use a fixed-point method:

$$\mathbf{D_{k+1}} = \left(\mathbf{G}^{\intercal}_{\mathbf{k}}\mathbf{C}^{-\mathbf{1}}_{\bar{\mathbf{D}}^{\text{obs}}}\mathbf{G_k}\right)^{-\mathbf{1}} \left(\mathbf{G}^{\intercal}_{\mathbf{k}}\mathbf{C}^{-\mathbf{1}}_{\bar{\mathbf{D}}^{\text{obs}}}\bar{\mathbf{D}}^{\text{obs}}\right) \tag{12}$$

where, $\mathbf{G_k}$ is just $\mathbf{G}$ evaluated at $\mathbf{D_k}$. Equation 12 typically converges within less than a dozen iterations.

Solution of Eq. 10 (via Eq. 12) allows us to infer the unknown structure-property model for GB diffusivity without knowing the form of the model *a priori*. Additionally, because the *a posteriori* information is represented by a probability density function, it is possible to quantify the uncertainty of the inference [45, 46], as will be explained in Section 2.4. We note, that in situations for which the *a posteriori* state of information is non-Gaussian, Eq. 9 may be solved using standard gradient-based or stochastic optimization algorithms. Also, the methods presented here are general and do not depend in any way on the piece-wise linear approximation employed.

2.4. Uncertainty Quantification

In addition to inferring the structure-property model that is most probable given the observed data, it is also desirable to quantify how much uncertainty exists in our inferred result (see [45, 46]). In technical terms, we seek to quantify the dispersion in $\sigma\left(\mathbf{D}, \mathbf{M}\right)$, resulting from the combined influence of the dispersion in all of the underlying models of the *a priori* states of information (including limitations due to measurement resolution). Here we make these ideas concrete and describe how we calculate the uncertainty before presenting our inference results together with their corresponding uncertainty.

Let us consider a simple example in which the domain of the structure-property model ($\mathscr{D}$) is discretized such that there are only two parameters (see Fig. 2b). For this example, the domain of

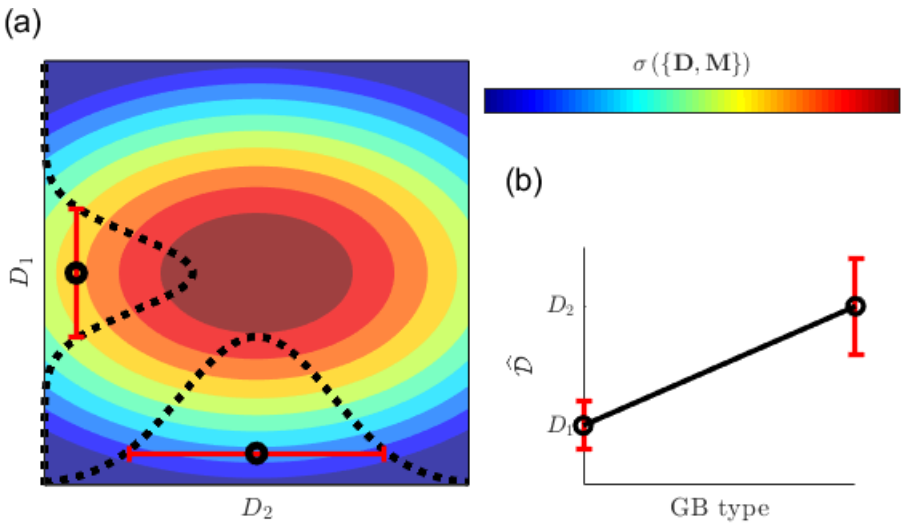

Figure 2: Illustration of the uncertainty quantification method. (a) Contour plot of $\sigma(\{\mathbf{D},\mathbf{M}\})$ with the marginal densities for each dimension shown as dotted lines. (b) The corresponding structure-property model ($\mathscr{D}$), discretized into two bins.

$\sigma(\mathbf{D},\mathbf{M})$ is two dimensional, so we can directly visualize it as the contour plot shown in Fig. 2a. Each point in the space shown in Fig. 2a represents a different candidate structure-property model, whose coordinates are the elements of $\mathbf{D}$ and provide the values of the structure-property model at specific points (see Fig. 2b). The color of the contour plot indicates the value of $\sigma(\mathbf{D},\mathbf{M})$, which represents the probability density that any structure-property model is consistent with the observed data, taking into account relevant uncertainties. Thus the model associated with the peak in Fig. 2a is the one that is most consistent with the observed data. The marginal density in each dimension (shown as dotted black lines in Fig. 2a) provides a measure of the uncertainty of the inferred value of the corresponding parameter. A straightforward quantification of the dispersion in the marginal distributions may be obtained by calculating the posterior covariance matrix. Which, for the present case of a Gaussian $\sigma(\mathbf{D},\mathbf{M})$, is given by [44]:

$$\widetilde{\mathbf{C}}_{\mathbf{D}} = \left(\mathbf{G}^{\intercal}\mathbf{C}^{-\mathbf{1}}_{\bar{\mathbf{D}}^{\text{obs}}}\mathbf{G}\right)^{-1} \tag{13}$$

The square roots of the diagonal elements, $\sqrt{\widetilde{C}^{jj}_{\mathbf{D}}}$, provide the standard deviations of the marginal distributions of each respective parameter (D_j), which we can show visually as the magnitudes of the error-bars as illustrated in Fig. 2b.

3. Results & Discussion

We considered both one-dimensional and three-dimensional constitutive models to validate our inference method. In the first case, we considered microstructures in which the crystallographic orientations of all grains shared a common $\langle 100\rangle$ axis and all GBs were of $\langle 100\rangle$ tilt character where the GB plane was ignored so that $\mathscr{D}$ was a one-dimensional function of ω. We refer to this as the one degree-of-freedom (1DOF) case. In the second case, we considered more general microstructures with arbitrary crystallographic orientations resulting in arbitrary disorientations, but we again ignored the influence of the GB plane so that $\mathscr{D}$ was a three-dimensional function of the angle (ω) and axis (θ,ϕ) of the disorientation. We refer to this as the three degree-of-freedom (3DOF) case. In the most general case, $\mathscr{D}$ is technically a second-rank tensor function encoding the anisotropic diffusivity in the plane of the GB and across it. If desired, inference of the elements of such a diffusivity tensor can be accomplished

using the methods described here. For now, we focus on the simple and illustrative case when $\mathscr{D}$ is assumed to be a scalar-valued function.

To validate our method, we first characterized the simulated 2D polycrystals to obtain the microstructural information, $\mathbf{M}$. Then, we obtained the observed effective diffusivity of the polycrystals, $\bar{\mathbf{D}}^{\text{obs}}$, by means of the method presented in Section 2.2. We then employed the proposed GB property localization method to infer $\mathscr{D}$ without considering any prior information about the true underlying structure-property model other than the fact that it is assumed to be non-negative. Validation of the inference method was then carried out by comparing the true constitutive model with the inference result. For each model, the inference was performed 50 times with different randomly selected sets of polycrystals, and the results presented correspond to the the inference with the median error over the 50 trials. For the 1DOF models, sets of 50 polycrystals were used; for the 3DOF models, sets of 110 polycrystals were used (both correspond to a 5:1 ratio of data to parameters).

3.1. 1DOF Validation Results

As mentioned previously, our discretization produces a piece-wise linear approximation to $\mathscr{D}$, which we will denote $\widehat{\mathscr{D}}$. In the 1DOF case we employed a uniform discretization with 5° resolution. We considered two different constitutive models for the 1DOF validation tests.

The first 1DOF constitutive model, as mentioned previously, was a modified version of the function developed by Bulatov, Reed, and Kumar to describe GB energy [7], which we linearly scaled and shifted to the range of realistic values of GB diffusivity for aluminum. Specifically, this transformation resulted in a model for which the minimum and maximum GB diffusivities were approximately equal to those employed in [47], which were extracted from the atomistic calculations of [48]. Our second 1DOF test employed the following analytical model:

$$\mathscr{D}(\omega) = D_{\text{high}} \exp\left[\left(\log\left(\frac{D_{\text{low}}}{D_{\text{high}}}\right)\right)\left(\left(\frac{4\omega}{\pi}\right) - 1\right)^4\right] \tag{14}$$

which is similar in form to results from experimental and computational surveys of diffusivity for $\langle 100 \rangle$ tilt GBs [49, 48]. In Eq. 14, D_{low} and D_{high} are the minimum and maximum diffusivities respectively, the values of which were the same as those employed in the 1DOF BRK model.

We make several notes about the constitutive models employed here. First, there is no existing structure-property model to predict GB diffusivity as a function of GB crystallography. Consequently, the models we have employed are not intended to be quantitatively accurate descriptions of actual GB diffusion processes, rather we have chosen models that possess qualitative features (e.g. the existence of singularities, diffusivity values that vary over many orders of magnitude) that reflect trends observed in the literature, in order to assess how well such features can be captured by the localization technique. Second, for the 1DOF case, the grain orientations assigned to the simulated polycrystals shared a common $\langle 100 \rangle$ rotation axis orthogonal to the sample surface, making all of the GBs $\langle 100 \rangle$ tilts. The first model we employed for $\mathscr{D}(\omega)$ is constructed by evaluating the full five degree-of-freedom BRK model over the one-dimensional submanifold corresponding to $\langle 110 \rangle$ symmetric tilt GBs. This submanifold was selected instead of the submanifold of $\langle 100 \rangle$ symmetric tilts because of the presence of a deeper cusp, which provides a clearer test of the inference method. The data that inspired the second 1DOF model were for $\langle 100 \rangle$ symmetric tilt GBs. Although all of the GBs in the 1DOF simulated microstructures are strictly $\langle 100 \rangle$ tilts, they are not all symmetric tilts, and, to make the model one-dimensional, we have ignored the GB plane altogether. Because we have ignored the GB plane, the domain of the disorientation angle is symmetric about 45°. Again, fidelity to the crystallography of the original data that inspired the

models was not our objective. Rather, regardless of their origin, we have selected/constructed models whose forms exhibit relevant features.

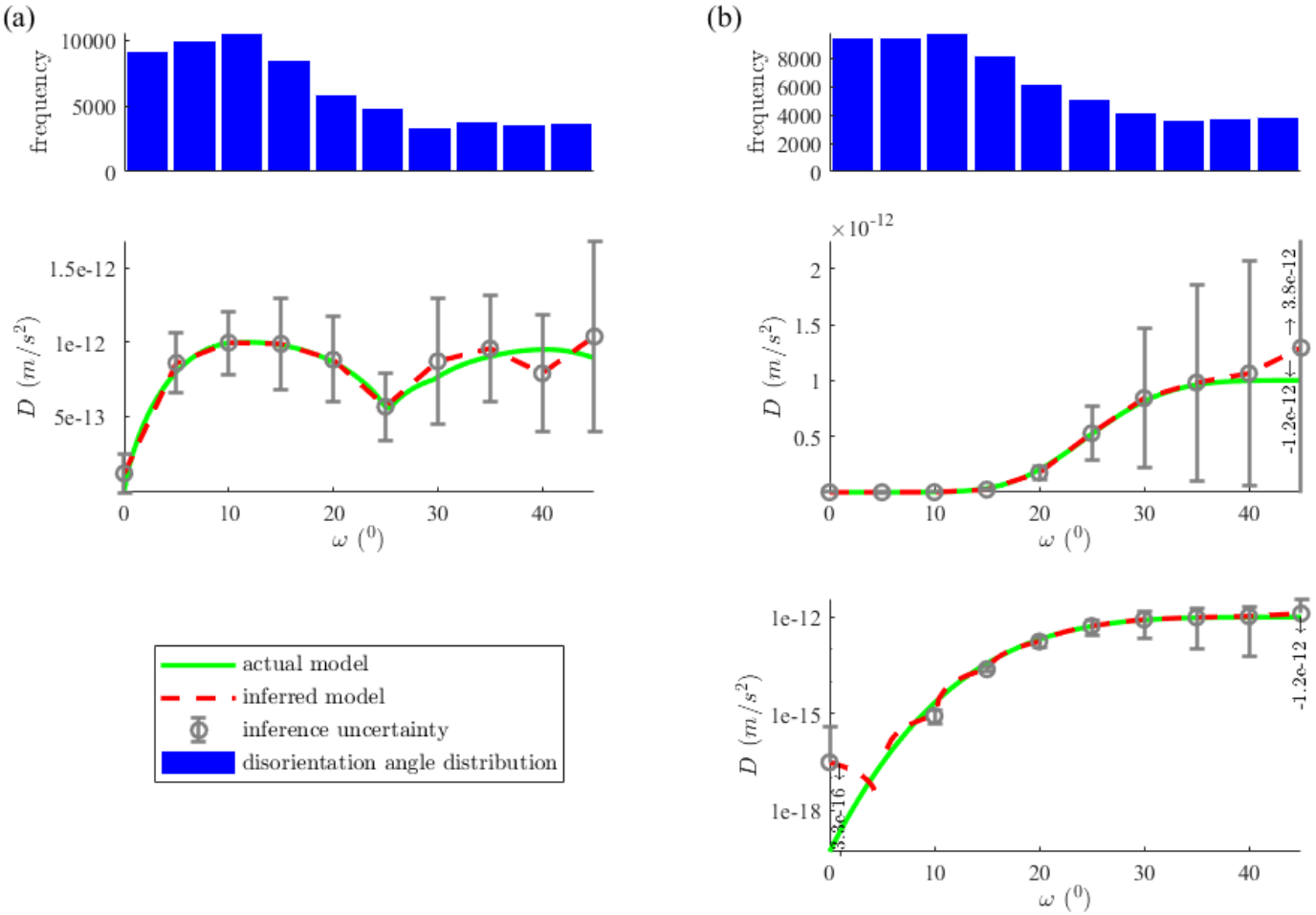

Figure 3: Comparison between the inferred model and the true model for (a) the 1DOF BRK function and (b) the exponential function of Eq. 14, together with quantified inference uncertainty. The inferred model shown is the one having the median error over 50 trials (inferences). The disorientation angle distribution across all of the employed microstructures is shown in histogram form above each plot. The bottom right plot is another view of the 1DOF exponential function, but with a logarithmically scaled vertical axis. Because of the logarithmic axis scaling, one zero valued point and two lower error bars that extend slightly below zero cannot be shown.

The localization results for both 1DOF models, together with the quantified uncertainty, can be seen in Fig. 3, where the green line is the model we attempted to infer (and which was ignored during the inference process). The red dashed line represents the piece-wise linear inference. The gray error bars indicate one standard deviation ($\sqrt{\widetilde{C}^{jj}_{\mathbf{D}}}$) in the marginal distribution of the respective parameter, which is our chosen metric to represent the uncertainty. Finally, the histogram shows the disorientation angle distribution across all of the microstructures employed in the inference. Note that with 50 randomly selected microstructures all of the bins contain a multiplicity of observations. Even with the coarse binning, and piece-wise linear representation, the results show very good agreement with the true models in both cases. In particular, we note that the localization inference successfully captured the singularity in the 1DOF BRK model (Fig. 3a). Figure 3b confirms that the method is also successful when the constitutive model spans many orders of magnitude. A quantitative discussion of the inference accuracy is presented later.

3.2. 3DOF Validation Result

For the 3DOF case, the GB property localization approach was validated against another modified version of the BRK energy function. In this case, instead of evaluating the BRK function along a submanifold, a three-dimensional constitutive model was constructed by integrating over the degrees of freedom corresponding to the GB plane:

$$\mathscr{D}(\omega,\theta,\phi) \propto \int_0^{2\pi}\int_0^{\frac{\pi}{2}} \mathrm{BRK}(\omega,\theta,\phi,\alpha,\beta)\sin\alpha \; \mathrm{d}\alpha \; \mathrm{d}\beta \tag{15}$$

In this 3DOF GB structure-property model, the diffusivity is a function of the disorientation angle (ω) and axis (θ,ϕ). Discretization of the disorientation fundamental zone (FZ) was carried out using the volumetric meshing capabilities of the Neper software package [50–53] with the Rodriguez space parameterization of the disorientation FZ supplied as the domain. The `-mesh3dalgo netg:gmne` meshing option was employed, which resulted in tetrahedral bins of approximately equal volume (see Fig. 4).

Figure 4a shows the results of the localization inference applied to the 3DOF model, using a piece-wise linear model constructed from a tetrahedral mesh with a total of 22 vertices (model parameters). In spite of the very coarse resolution employed (only 2.8 points per dimension), the agreement of the inference with the true model is decent. Figure 4b shows the uncertainty of the inference, quantified in the same way as the 1DOF case. We note that the uncertainty for the 3DOF case is similar in magnitude to the uncertainty in the 1DOF case. The 3DOF case shows that the localization method can be applied to a higher dimensional model and is encouraging for the ultimate goal of applying it to infer a structure-property model for GB diffusivity from experimental data as a function of all five degrees of freedom.

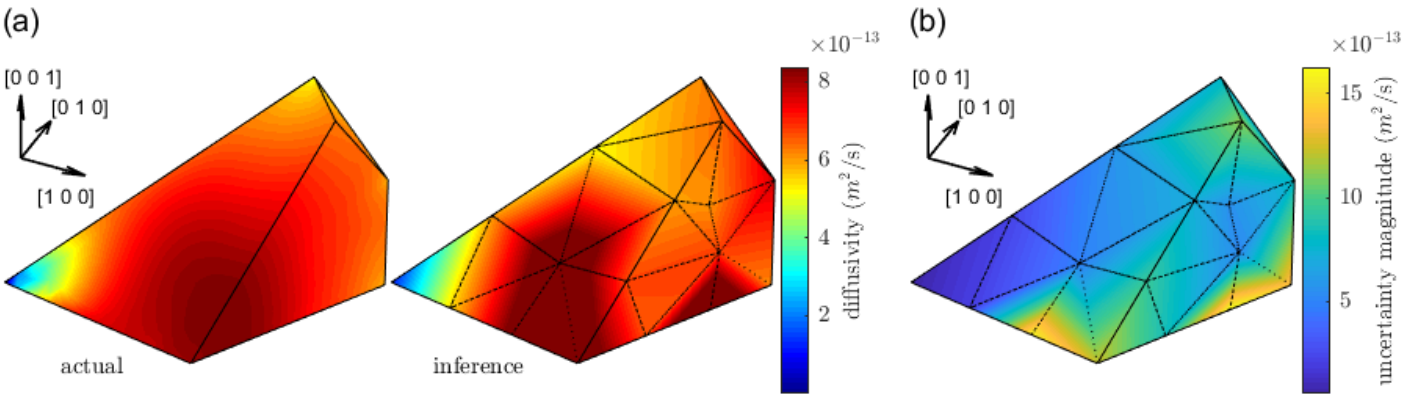

Figure 4: (a) Comparison between the true (left) and the inferred (right) 3DOF GB diffusivity structure-property model, displayed in the Rodriguez space parameterization of the disorientation fundamental zone (FZ). (b) The magnitude of the uncertainty (one standard deviation) in the inference. Interior lines define the boundaries of the tetrahedral bins used in the discretization.

The results just described demonstrate that the inverse problem theory approach to GB property localization can successfully infer a piece-wise linear approximation to an unknown structure-property model without the need for an *ansatz* of its analytical form.

3.3. Inference Accuracy

To quantify the accuracy of the inference results, we calculated the average integrated relative log error between the inferred model and the true model. Because the GB diffusivity structure-property models span orders of magnitude, care must be taken when computing differences. For example, a

deviation of 1 might be very small in a region where a function is on the order of 10^2, but could be very large in another region where that function is on the order of 10^{-2}. To address this issue, we calculate the error on a logarithmic scale:

$$\text{average integrated relative log error} = \frac{\int \left| \frac{\log\left(\widehat{\mathscr{D}}(\mathbf{\Omega}, \mathbf{D})\right) - \log\left(\mathscr{D}(\mathbf{\Omega})\right)}{\log\left(\mathscr{D}(\mathbf{\Omega})\right)} \right| \mathrm{d}\mathbf{\Omega}}{\int \mathrm{d}\mathbf{\Omega}} \tag{16}$$

where $\mathbf{\Omega} = \{\omega\}$ in the 1DOF case and $\mathbf{\Omega} = \{\omega, \theta, \phi\}$ in the 3DOF case and the domain as well as the differential volume element are chosen appropriately. In Eq. 16, $\widehat{\mathscr{D}}(\mathbf{\Omega}, \mathbf{D})$ represents the piece-wise linear approximation to $\mathscr{D}(\mathbf{\Omega})$ using the parameters in $\mathbf{D}$, and "log" denotes the natural logarithm. The average integrated relative log error describes the average error (across the entire domain) that would be expected in the logarithm of a prediction made using the inference result. The integration of Eq. 16 for 1DOF cases was carried out numerically using the trapezoidal rule. For the 3DOF case Monte-Carlo integration was employed [54].

The average integrated relative log error for each of the models, as shown in Table 1, was quite low, even for the 3DOF case, which employed a much coarser discretization than the 1DOF case (only 2.8 points per dimension, as opposed to 10 points for the 1DOF case) . To put these error measures in perspective, if the inferred model predicted a value of 5×10^{-13} m^2/s for the diffusivity of a particular GB, one could expect that the true value would be somewhere between 4.7×10^{-13} and 5.3×10^{-13} for the 1DOF BRK model, between 2.2×10^{-13} and 11.3×10^{-13} for the 1DOF exponential model, or between 4.6×10^{-13} and 5.4×10^{-13} for the 3DOF model.

model	average integrated relative log error
1DOF BRK	0.0023
1DOF Exponential (Eq. 14)	0.0287
3DOF	0.0028

Table 1: Average integrated relative log error of the inferred models.

3.4. Influence of Discretization Resolution and Number of Microstructures

To investigate the influence of discretization resolution, number of microstructures, and their interaction, we performed localization for the 1DOF BRK model using different numbers of parameters and microstructures. As can be seen in Fig. 5, for a fixed number of microstructures, the finer the resolution of the discretization (i.e. the more parameters that were employed) the lower the error in the inference, as expected. However, there also appears to be a number of parameters above which the reduction of the error is not significant (approximately 10 for large numbers of microstructures). Consistent with intuition, for a fixed number of parameters, the use of more microstructures also leads to improved inference. However, we again observe a saturation point at a certain number of microstructures (around 50 in the present case, which is the reason that 50 microstructures—or a 5:1 data to parameter ratio—were used in the results of Section 3), above which there is little added benefit.

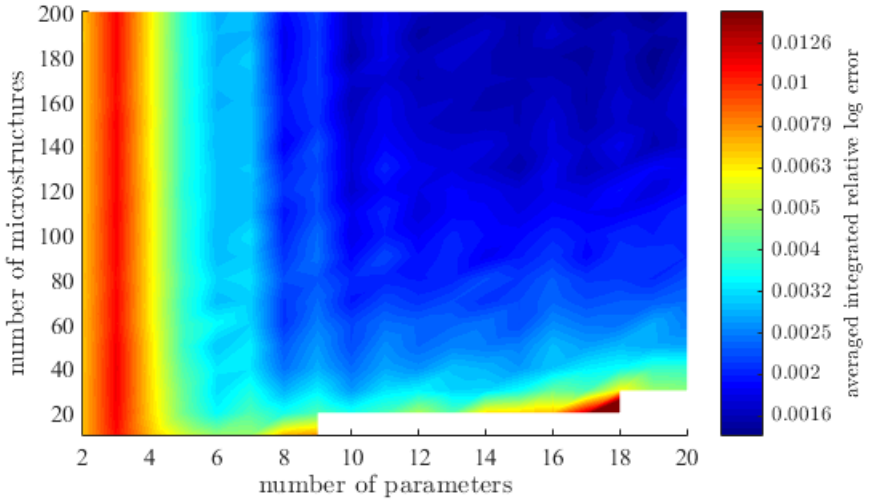

Figure 5: Comparison of the average integrated relative log error of the inference using different numbers of parameters and microstructures. In this comparison, we used the 1DOF BRK model. The white region corresponds to underdetermined (or close to underdetermined) points, for which methods in the sequel to this paper should be employed to make meaningful inferences.

4. Conclusion

In this work, we developed a Bayesian approach to GB property localization that enables the inference of a GB structure-property model when the only available data are measurements of the effective properties of polycrystals, and when the form of the model is unknown *a priori*. We considered the case when the number of observations is greater than the number of parameters to be inferred. The method is robust to and rigorously incorporates measurement uncertainty. We tested the method for 1DOF and 3DOF cases and observed satisfactory inference accuracy, even using a relatively coarse discretization. We also demonstrated how uncertainty quantification for the inference result is naturally included in the method.

While GB diffusivity was the focus of the present work, the property localization inference method presented here should also be applicable to other properties of interest for which a suitable homogenization relation is available.

Acknowledgement

The material presented here is based upon work supported by the National Science Foundation under Grant No. 1610077. We thank Jarrod M. Lund and Tyler R. Critchfield for their assistance in developing the Monte Carlo code to assign grain orientations for the two dimensional polycrystal templates. We would also like to show our gratitude for the guidance and insights from David Page and Akash Amalaraj during the course of this research.

A. Derivation of Diffusivity Homogenization Equation

The derivation of Eq. 1 is related to the idea of [40] that one can obtain the effective diffusivity from Fick's First law by considering the flux across some "slice" through the microstructure. However, in contrast to [40], we are interested in the effective diffusivity of the entire GBN, rather than the average diffusivity of individual GBs in the network; the two ideas are, nevertheless, intimately related (see

footnote 1 in [26]). Our approach to calculate the effective diffusivity of the entire GBN is equivalent to an adaptation of the finite volume method (see [27]). For convenience, we set the concentration at the source node (node a) to be c_0 and consider the total flux ($J_b = Q_b/A$) arriving at the sink node (node b), whose concentration we fix at 0 (Neumann boundary conditions). The effective diffusivity is then

$$\bar{D}^{\text{pred}} = \frac{L}{c_0}\frac{Q_b}{A} \tag{17}$$

and the mass flow rate arriving at the sink is simply

$$Q_b = \sum_{i\sim b} -\frac{D_{ib}A_{ib}}{L_{ib}}\left(c_b - c_i\right) \tag{18}$$

where D_{ib}, A_{ib}, and L_{ib} are, respectively, the diffusivity, cross-sectional area, and length of the edge connecting node i to node b, c_k is the concentration at node k, and the sum is over all edges in the GBN that are incident to node b ($i \sim b$ denotes that there is an edge between nodes i and b). Making use of the definition of the GBN Laplacian matrix ($\mathcal{L}$) [27], this can be rewritten as

$$Q_b = -\mathcal{L}_b^{\intercal} c \tag{19}$$

where $\mathcal{L}_b$ is the b-th column of $\mathcal{L}$ and c is a vector containing the concentration at every node, which is calculated by solving the linear system of equations defined by

$$\widehat{\mathcal{L}} c = c_0 e_b \tag{20}$$

where $\widehat{\mathcal{L}}$ is a matrix formed by replacing the a-th and b-th rows of $\mathcal{L}$ with $e_a^{\intercal}$ and $e_b^{\intercal}$ respectively, and where e_k is a vector having the k-th element equal to one and all others equal to zero. We note that Eq. 20 is simply a statement of conservation of mass at every node. Substituting the solution of Eq. 20 into Eq. 19 and substituting the result into Eq. 17 we arrive at Eq. 1. We note also that the direct inversion of $\widehat{\mathcal{L}}$ is not necessary for the solution of Eq. 20, and is not computationally efficient; rather, standard methods for the solution of linear systems of equations will be preferred. In our implementation of Eq. 1 we employ MATLAB's `mldivide` operator.

B. Inverse Problem Theory

Here we give a brief overview of relevant aspects of Tarantola's approach to Bayesian inverse problem theory, and then demonstrate its application to the problem of GB property localization. Inverse problem theory is a method of inferring model parameters ($\mathbf{x}$) that characterize a system using the results of some measurements/observations of the system ($\mathbf{y}$) [44, 42, 43, 45, 46]. In a given system, $\mathbf{x} = \{x_1, x_2, \dots\}$ is a set containing the independent parameters and $\mathbf{y} = \{y_1, y_2, \dots\}$ is a set containing the dependent parameters, both of which we may only hope to know with some imperfect degree of certainty. Tarantola[5] proposed that our state of information (what we know about $\mathbf{y}$ and $\mathbf{x}$) can be described by a PDF, called the *a posteriori* state of information, $\sigma(\mathbf{y}, \mathbf{x})$, which is equal to the conjunction of the *a priori* state of information, $\rho(\mathbf{y}, \mathbf{x})$, and the theoretical state of information, $\Theta(\mathbf{y}, \mathbf{x})$ [44]. The *a priori* state

[5] It is worth noting that a useful alternative Bayesian formulation of inverse problems exists, as described by [45, 46], which results in a conditional *a posteriori* density $\sigma(\mathbf{x}|\mathbf{y})$. We have chosen to follow the approach introduced by Tarantola [44], which results in the joint *a posteriori* density $\sigma(\mathbf{y}, \mathbf{x})$ and avoids the, perhaps rare, mathematical singularity that can exist in $\sigma(\mathbf{x}|\mathbf{y})$ for events with vanishing probability (Borel's paradox).

of information is what we know before ever making any observations and may represent some known physical constraints. The theoretical state of information encodes correlations between $\mathbf{x}$ and $\mathbf{y}$ resulting from a homogenization or other physical theory and corresponding uncertainty. Using the Kolmogorov axioms, Tarantola and Valette showed that the *a posteriori* state of information is given by [42]:

$$\sigma(\mathbf{y},\mathbf{x}) = k\frac{\rho(\mathbf{y},\mathbf{x})\Theta(\mathbf{y},\mathbf{x})}{\mu(\mathbf{y},\mathbf{x})} \tag{21}$$

Here, k is a normalization constant, and $\mu(\mathbf{y},\mathbf{x})$ is the homogeneous state of information, which is the PDF that assigns a probability to each region of the parameter space that is equal to the volume of that region [43]. Functionally, $\mu(\mathbf{y},\mathbf{x})$ represents a state of complete ignorance (i.e. the absence of any *a priori* information), so that the ratio in Eq. 21 can be interpreted as quantifying how much is known relative to a state of complete ignorance. In the present context, Eq. 1 represents the forward problem, where the dependent parameter is the observed effective diffusivity $\mathbf{y} = \{\bar{\mathbf{D}}^{\text{obs}}\}$ and the independent parameters are the structure-property model and sample microstructure $\mathbf{x} = \{\mathscr{D}, \mathbf{M}\}$. As described in Section 2.3, GB property localization will typically leverage information from multiple samples, so that we have $\mathbf{M} = \{M_1, M_2, ..., M_N\}$ and $\bar{\mathbf{D}}^{\text{obs}} = \{\bar{D}_1^{\text{obs}}, \bar{D}_2^{\text{obs}}, ..., \bar{D}_N^{\text{obs}}\}$. Ignoring the normalization constant, we can then rewrite Eq. 21 as:

$$\sigma(\bar{\mathbf{D}}^{\text{obs}}, \mathscr{D}, \mathbf{M}) \propto \frac{\rho(\bar{\mathbf{D}}^{\text{obs}}, \mathscr{D}, \mathbf{M})\Theta(\bar{\mathbf{D}}^{\text{obs}}, \mathscr{D}, \mathbf{M})}{\mu(\bar{\mathbf{D}}^{\text{obs}}, \mathscr{D}, \mathbf{M})} \tag{22}$$

The resolution of the inverse problem consists in identifying the structure-property model, $\mathscr{D}$, that is most probable given our observations of $\bar{\mathbf{D}}^{\text{obs}}$ and $\mathbf{M}$. This is accomplished by integrating Eq. 22 to compute the *a posteriori* state of information over the space of independent parameters:

$$\sigma(\mathscr{D}, \mathbf{M}) = \int \sigma(\bar{\mathbf{D}}^{\text{obs}}, \mathscr{D}, \mathbf{M}) d(\bar{\mathbf{D}}^{\text{obs}}) \tag{23}$$

The evaluation of this integral is facilitated by considering relevant simplifications. Because the *a priori* information about $\mathbf{M}$ and $\mathscr{D}$ is not obtained from measurements of $\bar{\mathbf{D}}^{\text{obs}}$, their states of information are independent [44], which implies that:

$$\rho(\bar{\mathbf{D}}^{\text{obs}}, \mathscr{D}, \mathbf{M}) = \rho_{\bar{\mathbf{D}}^{\text{obs}}}(\bar{\mathbf{D}}^{\text{obs}})\rho_{\{\mathscr{D},\mathbf{M}\}}(\mathscr{D}, \mathbf{M}) \tag{24}$$

$$\mu(\bar{\mathbf{D}}^{\text{obs}}, \mathscr{D}, \mathbf{M}) = \mu_{\bar{\mathbf{D}}^{\text{obs}}}(\bar{\mathbf{D}}^{\text{obs}})\mu_{\{\mathscr{D},\mathbf{M}\}}(\mathscr{D}, \mathbf{M}) \tag{25}$$

It should be noted here that subscripts are used to distinguish the functions.

Let us assume that Eq. 1, as the physical theory relating the independent and dependent parameters, is at most mildly[6] non-linear. Combining this assumption with the Kolmogorov definition for conditional probability [55], and taking the homogeneous probability of the independent parameters as their marginal probability, $\Theta(\bar{\mathbf{D}}^{\text{obs}}, \mathscr{D}, \mathbf{M})$ can be written, according to the treatment of Tarantola and Vallete [44, 42], as:

$$\Theta(\bar{\mathbf{D}}^{\text{obs}}, \mathscr{D}, \mathbf{M}) = \theta\left(\bar{\mathbf{D}}^{\text{obs}} \mid \{\mathscr{D}, \mathbf{M}\}\right)\mu_{\{\mathscr{D},\mathbf{M}\}}(\mathscr{D}, \mathbf{M}) \tag{26}$$

Substituting Eqs. 22 and 24–26 into Eq. 23, we obtain:

[6] This is rather flexible, and we find that in some cases even strongly non-linear theoretical relations can be considered.

$$\sigma\left(\mathscr{D},\mathbf{M}\right) \propto \rho_{\{\mathscr{D},\mathbf{M}\}}\left(\mathscr{D},\mathbf{M}\right) \int \frac{\rho_{\bar{\mathbf{D}}^{\text{obs}}}(\bar{\mathbf{D}}^{\text{obs}})\theta\left(\bar{\mathbf{D}}^{\text{obs}} \mid \{\mathscr{D},\mathbf{M}\}\right)}{\mu_{\bar{\mathbf{D}}^{\text{obs}}}(\bar{\mathbf{D}}^{\text{obs}})} d(\bar{\mathbf{D}}^{\text{obs}}) \tag{27}$$

Because the manifold that $\bar{\mathbf{D}}^{\text{obs}}$ inhabits is a linear space, using the definition of homogeneous probability distribution presented by Mosegaard and Tarantola [43], $\mu(\bar{\mathbf{D}}^{\text{obs}})$ is constant. We also make the simplifying approximation that any uncertainty in Eq. 1 is negligible, which implies that $\theta\left(\bar{\mathbf{D}}^{\text{obs}} \mid \{\mathscr{D},\mathbf{M}\}\right) = \delta(\bar{\mathbf{D}}^{\text{obs}} - \bar{\mathbf{D}}^{\text{pred}}(\mathscr{D},\mathbf{M}))$. Under these conditions, the integration operation in Eq. 27 results in:

$$\sigma(\mathscr{D},\mathbf{M}) \propto \rho_{\{\mathscr{D},\mathbf{M}\}}\left(\mathscr{D},\mathbf{M}\right) \rho_{\bar{\mathbf{D}}^{\text{obs}}}\left(\bar{\mathbf{D}}^{\text{pred}}(\mathscr{D},\mathbf{M})\right) \tag{28}$$

which is the result given in Eq. 3. The last term, $\rho_{\bar{\mathbf{D}}^{\text{obs}}}\left(\bar{\mathbf{D}}^{\text{pred}}(\mathscr{D},\mathbf{M})\right)$, is a likelihood function, which quantifies how well the model explains the data. In other words, $\rho_{\bar{\mathbf{D}}^{\text{obs}}}\left(\bar{\mathbf{D}}^{\text{pred}}(\mathscr{D},\mathbf{M})\right)$ quantifies how well the independent parameters explain the dependent parameters. Thus, for the conditions presented here, the *a posteriori* state of information about the independent parameters is proportional to the product of the likelihood function and the *a priori* state of information about the independent parameters.

References

[1] I. Kaur, Y. Mishin, W. Gust, Fundamentals of Grain and Interphase Boundary Diffusion, 3rd Edition, Willey, 1995.

[2] R. C. Hugo, R. G. Hoagland, The Kinetics of Gallium Penetration into Aluminum Grain Boundaries - in situ TEM Observations and Atomistic Models, Acta Materialia 48 (8) (2000) 1949–1957. doi:10.1016/S1359-6454(99)00463-2.

[3] D. L. Olmsted, S. M. Foiles, E. A. Holm, Survey of computed grain boundary properties in face-centered cubic metals: I. Grain boundary energy, Acta Materialia 57 (13) (2009) 3694–3703. doi:10.1016/j.actamat.2009.04.007.
URL http://dx.doi.org/10.1016/j.actamat.2009.04.007

[4] D. L. Olmsted, E. A. Holm, S. M. Foiles, Survey of computed grain boundary properties in face-centered cubic metals-II: Grain boundary mobility, Acta Materialia 57 (13) (2009) 3704–3713. doi:10.1016/j.actamat.2009.04.015.
URL http://dx.doi.org/10.1016/j.actamat.2009.04.015

[5] A. D. Rollett, C. C. Yang, W. W. Mullins, B. L. Adams, C. T. Wu, D. Kinderlehrer, S. Ta'asan, F. Manolache, C. Liu, I. Livshits, D. Mason, A. Talukder, S. Ozdemir, D. Casasent, A. Morawiec, D. Saylor, G. S. Rohrer, M. Demirel, B. El-Dasher, W. Yang, Grain Boundary Property Determination through Measurement of Triple Junction Geometry and Crystallography, Recrystallization and Grain Growth, Vols 1 and 2 (2001) 165–175.
URL <GotoISI>://WOS:000175295500015

[6] W. T. Read, W. Shockley, Dislocation Models of Crystal Grain Boundaries, Physical Review 78 (3) (1950) 275–289.

[7] V. V. Bulatov, B. W. Reed, M. Kumar, Grain boundary energy function for fcc metals, Acta Materialia 65 (2014) 161–175. doi:10.1016/j.actamat.2013.10.057.
URL http://dx.doi.org/10.1016/j.actamat.2013.10.057

[8] M. Binci, D. Fullwood, S. R. Kalidindi, A new spectral framework for establishing localization relationships for elastic behavior of composites and their calibration to finite-element models, Acta Materialia 56 (10) (2008) 2272–2282. doi:10.1016/j.actamat.2008.01.017.

[9] T. Fast, S. R. Kalidindi, Formulation and calibration of higher-order elastic localization relationships using the MKS approach, Acta Materialia 59 (11) (2011) 4595–4605. doi:10.1016/j.actamat.2011.04.005.
URL http://dx.doi.org/10.1016/j.actamat.2011.04.005

[10] D. T. Fullwood, S. R. Kalidindi, B. L. Adams, S. Ahmadi, A Discrete Fourier Transform Framework for Localization Relations, Computers, Materials and Continua 9 (1) (2009) 25–39. doi:10.3970/cmc.2009.009.025.

[11] S. R. Kalidindi, G. Landi, D. T. Fullwood, Spectral representation of higher-order localization relationships for elastic behavior of polycrystalline cubic materials, Acta Materialia 56 (15) (2008) 3843–3853. doi:10.1016/j.actamat.2008.01.058.

[12] G. Landi, S. R. Kalidindi, Thermo-Elastic Localization Relationships for Multi-Phase Composites, Computers, Materials and Continua 16 (3) (2010) 273–293. doi:10.3970/cmc.2010.016.273.

[13] Y. C. Yabansu, D. K. Patel, S. R. Kalidindi, Calibrated localization relationships for elastic response of polycrystalline aggregates, Acta Materialia 81 (2014) 151–160. doi:10.1016/j.actamat.2014.08.022.
URL http://dx.doi.org/10.1016/j.actamat.2014.08.022

[14] Y. C. Yabansu, S. R. Kalidindi, Representation and calibration of elastic localization kernels for a broad class of cubic polycrystals, Acta Materialia 94 (2015) 26–35. doi:10.1016/j.actamat.2015.04.049.
URL http://dx.doi.org/10.1016/j.actamat.2015.04.049

[15] D. Y. Li, J. A. Szpunar, Determination of Single Crystals' Elastic Constants from the Measurement of Ultrasonic Velocity in the Polycrystalline Material, Acta Metallurgica Et Materialia 40 (12) (1992) 3277–3283. doi:10.1016/0956-7151(92)90041-C.

[16] M. Hayakawa, S. Imai, M. Oka, Determination of Single-Crystal Elastic Constants from a Cubic Polycrystalline Aggregate, Journal of Applied Crystallography 18 (1985) 513–518. doi:10.1107/S0021889885010809.

[17] D. K. Patel, H. F. Al-Harbi, S. R. Kalidindi, Extracting single-crystal elastic constants from polycrystalline samples using spherical nanoindentation and orientation measurements, Acta Materialia 79 (2014) 108–116. doi:10.1016/j.actamat.2014.07.021.

[18] L. Gold, Evaluation of the Stiffness Coefficients for Beryllium from Ultrasonic Measurements in Polycrystalline and Single Crystal Specimens, Physical Review 77 (3) (1950) 390–395. doi:10.1103/PhysRev.77.390.

[19] S. I. Wright, Estimation of Single-Crystal Elastic Constants from Textured Polycrystal Measurements, Journal of Applied Crystallography 27 (5) (1994) 794–801. doi:10.1107/S0021889894001883.
URL http://scripts.iucr.org/cgi-bin/paper?S0021889894001883

[20] T. Gnäupel-Herold, P. C. Brand, H. J. Prask, Calculation of Single-Crystal Elastic Constants for Cubic Crystal Symmetry from Powder Diffraction Data, Journal of Applied Crystallography 31 (6) (1998) 929–935. doi:10.1107/S002188989800898X.

[21] P. Haldipur, F. J. Margetan, R. B. Thompson, Estimation of Single-Crystal Elastic Constants from Ultrasonic Measurements on Polycrystalline Specimens, AIP Conference Proceedings 700 (2004) (2004) 1061–1068. doi:10.1063/1.1711735.
URL http://aip.scitation.org/doi/abs/10.1063/1.1711735

[22] P. Haldipur, F. J. Margetan, R. B. Thompson, Estimation of Single-Crystal Elastic Constants of Polycrystalline Materials from Back-Scattered Grain Noise, AIP Conference Proceedings 820 II (2006) (2006) 1133–1140. doi:10.1063/1.2184652.

[23] D. Gasteau, N. Chigarev, L. Ducousso-Ganjehi, V. E. Gusev, F. Jenson, P. Calmon, V. Tournat, Single crystal elastic constants evaluated with surface acoustic waves generated and detected by lasers within polycrystalline steel samples, Journal of Applied Physics 119 (4) (2016) 043103. doi:10.1063/1.4940367.

[24] X. Du, J. C. Zhao, Facile measurement of single-crystal elastic constants from polycrystalline samples, npj Computational Materials 3 (1) (2017) 1–7. doi:10.1038/s41524-017-0019-x.
URL http://dx.doi.org/10.1038/s41524-017-0019-x

[25] G. Sha, A simultaneous non-destructive characterisation method for grain size and single-crystal elastic constants of cubic polycrystals from ultrasonic measurements, Insight: Non-Destructive Testing and Condition Monitoring 60 (4) (2018) 190–193. doi:10.1784/insi.2018.60.4.190.

[26] O. K. Johnson, L. Li, M. J. Demkowicz, C. A. Schuh, Inferring grain boundary structure-property relations from effective property measurements, Journal of Materials Science 50 (21) (2015) 6907–6919. doi:10.1007/s10853-015-9241-4.
URL http://link.springer.com/10.1007/s10853-015-9241-4

[27] O. K. Johnson, J. M. Lund, T. R. Critchfield, Spectral graph theory for characterization and homogenization of grain boundary networks, Acta Materialia 146 (2018) 42–54. doi:10.1016/j.actamat.2017.11.054.

[28] E. A. Lazar, R. D. MacPherson, D. J. Srolovitz, A more accurate two-dimensional grain growth algorithm, Acta Materialia 58 (2009) 364–372. doi:10.1016/j.actamat.2009.09.008.
URL http://ac.els-cdn.com/S135964540900603X/1-s2.0-S135964540900603X-main.pdf?_tid=3270f958-8c31-11e7-9c9a-00000aacb361&acdnat=1503953038_1e46c1df84489139c05785710d1ce186

[29] M. Frary, C. A. Schuh, Grain boundary networks: Scaling laws, preferred cluster structure, and their implications for grain boundary engineering, Acta Materialia 53 (16) (2005) 4323–4335. doi:10.1016/j.actamat.2005.05.030.

[30] V. Y. Gertsman, K. Tangri, Computer Simulation Study of Grain Boundary and Triple Junction Distributions in Microstructures Formed by Mupltiple Twinning, Acta metall, mater. 43 (6) (1995) 2317–2324.

[31] O. K. Johnson, C. A. Schuh, The uncorrelated triple junction distribution function: Towards grain boundary network design, Acta Materialia 61 (8) (2013) 2863–2873. doi:10.1016/j.actamat.2013.01.025.

[32] P. Fortier, W. A. Miller, K. T. Aust, Triple Junction and Grain Boundary Character Distributions in Metallic Materials, Acta mater. 45 (8) (1997) 4–9.

[33] Y. S. Yi, J. S. Kim, Characterization methods of grain boundary and triple junction distributions, Scripta Materialia 50 (6) (2004) 855–859. doi:10.1016/j.scriptamat.2003.12.010.

[34] P. Davies, V. Randle, G. Watkins, H. Davies, Triple junction distribution profiles as assessed by electron backscatter diffraction, Journal of Materials Science 37 (19) (2002) 4203–4209. doi:10.1023/A:1020052306493.

[35] A. D. Rollett, K. Barmak, Orientation Mapping, in: Physical Metallurgy, Elsevier, 2014, pp. 1113–1141. doi:10.1016/B978-0-444-53770-6.00011-3.
URL https://www.sciencedirect.com/science/article/pii/B9780444537706000113{#}bib14https://linkinghub.elsevier.com/retrieve/pii/B9780444537706000113

[36] I. Brough, P. S. Bate, F. J. Humphreys, Optimising the angular resolution of EBSD, Materials Science and Technology 22 (11) (2006) 1279–1286. doi:10.1179/174328406X130902.
URL http://www.tandfonline.com/doi/full/10.1179/174328406X130902

[37] S. Zaefferer, On the formation mechanisms, spatial resolution and intensity of backscatter Kikuchi patterns, Ultramicroscopy 107 (2-3) (2007) 254–266. doi:10.1016/j.ultramic.2006.08.007.
URL https://www.sciencedirect.com/science/article/pii/S030439910600163Xhttps://linkinghub.elsevier.com/retrieve/pii/S030439910600163X

[38] J. Kacher, C. Landon, B. L. Adams, D. Fullwood, Bragg's Law diffraction simulations for electron backscatter diffraction analysis, Ultramicroscopy 109 (9) (2009) 1148–1156. doi:10.1016/j.ultramic.2009.04.007.
URL http://www.ncbi.nlm.nih.gov/pubmed/19520512https://linkinghub.elsevier.com/retrieve/pii/S0304399109001132

[39] A. J. Wilkinson, G. Meaden, D. J. Dingley, High-resolution elastic strain measurement from electron backscatter diffraction patterns: New levels of sensitivity, Ultramicroscopy 106 (4-5) (2006) 307–313. doi:10.1016/j.ultramic.2005.10.001.
URL https://www.sciencedirect.com/science/article/pii/S0304399105002251https://linkinghub.elsevier.com/retrieve/pii/S0304399105002251

[40] Y. Chen, C. A. Schuh, Diffusion on grain boundary networks: Percolation theory and effective medium approximations, Acta Materialia 54 (18) (2006) 4709–4720. doi:10.1016/j.actamat.2006.06.011.

[41] M. M. Moghadam, J. M. Rickman, M. P. Harmer, H. M. Chan, The role of boundary variability in polycrystalline grain-boundary diffusion, Journal of Applied Physics 117 (4) (2015) 045311. doi:10.1063/1.4906778.
URL http://dx.doi.org/10.1063/1.4906778

[42] A. Tarantola, B. Valette, Inverse Problems = Quest for Information, Journal of Geophysics 50 (3) (1982) 159–170. doi:10.1038/nrn1011.
URL http://www.ipgp.fr/~tarantola/Files/Professional/Papers_PDF/IP_QI_latex.pdf

[43] K. Mosegaard, A. Tarantola, Probabilistic Approach to Inverse Problems, in: International Handbook of Earthquake & Engineering Seismology (Part A), Academic Press, 2002, pp. 237–265. doi:10.1016/S0074-6142(02)80219-4.

[44] A. Tarantola, Inverse Problem Theory and Methods for Model Parameter Estimation, Society for Industrial and Applied Mathematics, Philadelphia, 2005.

[45] R. Aggarwal, M. J. Demkowicz, Y. M. Marzouk, Bayesian inference of substrate properties from film behavior, Modelling and Simulation in Materials Science and Engineering 23 (1) (2015) 0–15. doi:10.1088/0965-0393/23/1/015009.

[46] R. Aggarwal, M. J. Demkowicz, Y. M. Marzouk, Information-Driven Experimental Design in Materials Science, in: Information Science for Materials Discovery and Design, Vol. 225, Springer, 2016, pp. 13 – 44. doi:10.1007/978-3-319-23871-5.

[47] O. K. Johnson, C. A. Schuh, Texture mediated grain boundary network design in three dimensions, Mechanics of Materials 118 (2018) 94–105. doi:10.1016/j.mechmat.2017.12.001.
URL https://doi.org/10.1016/j.mechmat.2017.12.001

[48] M. Biscondi, Intergranular diffusion and grain-boundary structure, in: P. Lacombe (Ed.), Physical Chemistry of the Solid State: Applications to Metals and their Compounds, Elsevier Science Publishers B.V., Amsterdam, 1984, pp. 225–239.

[49] J. Sommer, C. Herzig, S. Mayer, W. Gust, Grain Boundary Self-Diffusion in Silver Bicrystals, Defect and Diffusion Forum 66-69 (1989) 843–848.

[50] R. Quey, P. R. Dawson, F. Barbe, Large-scale 3D random polycrystals for the finite element method: Generation, meshing and remeshing, Computer Methods in Applied Mechanics and Engineering 200 (17-20) (2011) 1729–1745. doi:10.1016/j.cma.2011.01.002.
URL http://dx.doi.org/10.1016/j.cma.2011.01.002

[51] R. Quey, Neper Reference Manual; The documentation for Neper 3.0.2; A software package for polycrystal generation and meshing (2017).
URL http://neper.sourceforge.net/

[52] R. Quey, L. Renversade, Optimal polyhedral description of 3D polycrystals: Method and application to statistical and synchrotron X-ray diffraction data, Computer Methods in Applied Mechanics and Engineering 330 (2018) 308–333. doi:10.1016/j.cma.2017.10.029.

[53] R. Quey, Polycrystal Generation and Meshing — Neper 3.0.2.
URL http://neper.sourceforge.net/

[54] S. Weinzierl, Introduction to Monte Carlo methods (2000). arXiv:0006269.

[55] A. N. Kolmogorov, Foundations of the Theory of Probability, Second English Edition, Chelsea Publishing Company, New York, NY, USA, 1956, English translation edited by Nathan Morrison.